Facile fabrication of novel SiO$_2$/g-C$_3$N$_4$ core–shell nanosphere photocatalysts with enhanced visible light activity

Bo Lin[a], Chao Xue[a], Xiaoqing Yan[a], Guidong Yang[a,*], Guang Yang[b], Bolun Yang[a]

[a] Department of Chemical Engineering, School of Chemical Engineering and Technology, Xi'an Jiaotong University, Xi'an 710049, PR China
[b] Electronic Materials Research Laboratory, Key Laboratory of the Ministry of Education & International Center for Dielectric Research, Xi'an Jiaotong University, Xi'an 710049, PR China

ARTICLE INFO

ABSTRACT

Novel SiO$_2$/g-C$_3$N$_4$ core–shell nanospheres were simply synthesized using heating method to anneal the mixture of silica dioxide nanospheres and molten cyanamide (CA) in nitrogen atmosphere. The effects of various initial mass ratios of SiO$_2$ nanospheres and CA molecules on the catalyst structure, surface property and catalytic activity have been systematically investigated. The characterization results show that the as-obtained photocatalysts possess the ordered core–shell nanostructure, large mesoporous distribution and inflated BET specific surface areas. The photocatalytic activities of the SiO$_2$/g-C$_3$N$_4$ composites were evaluated by decomposing the rhodamine B (RhB) dye under visible light irradiation. Compared with pure g-C$_3$N$_4$, all of the SiO$_2$/g-C$_3$N$_4$ core–shell composites showed the improved photoactivity, and the optimal SiO$_2$/g-C$_3$N$_4$ catalyst (SC-3) showed the highest activity with an RhB conversion of 94.3% after 150 min visible light irradiation, which is 3.5 times higher than that of pure g-C$_3$N$_4$. Meanwhile, the recycling test showed that the SC-3 sample owns outstanding stability and durability. The enhancement in both activity and stability can be assigned to the specific core–shell structure, inflated surface area, higher visible light adsorption and efficient charge separation originating from the closely contacted interfaces between SiO$_2$ nanospheres and g-C$_3$N$_4$.

© 2015 Elsevier B.V. All rights reserved.

1. Introduction

With the tremendous consumption of fossil-fuel reserves, a severe and vexing challenge is to seek a renewable and clean energy resource and insure the security of energy supply worldwide [1]. Solar power, which possesses enormous potential as a clean, abundant and economical energy, may be the most optimal solution to overcome the hard problem of energy shortage. In order to take advantage of solar energy fully and efficiently, great efforts have been made in the past decades, especially in photocatalytic field [2–4]. As is well known, the development of novel photocatalysts with high quantum efficiency is an effective and feasible direction for the utilization of solar energy. Graphitic carbon nitride (g-C$_3$N$_4$), as a new form of organic polymer-like semiconductor photocatalytic material, has attracted increasing attention because of its outstanding optical, electronic, morphological and catalytic properties [5–7]. Besides, compared with other allotrope of carbon nitride, g-C$_3$N$_4$ shows the most stable structure because of the

formation of strong covalent bonds between carbon and nitride atoms [8,9]. Most importantly, the g-C$_3$N$_4$ material has a large advantage that can be excited by visible light due to its narrow optical band gap of about 2.7 eV [6]. Meanwhile, it also can be facilely synthesized from various available precursors, such as cyanamide [10], dicyandiamide [11], melamine [12], urea and thiourea [13], etc. It is therefore induced that all of the above-mentioned specific properties make the g-C$_3$N$_4$ material become a potential candidate in various applications, for example, the purification of contaminated water [14], hydrogen evolution [15], energy storage [16], humidity and gas sensors [17,18] and solar cells [19], etc.

However, a major barrier to the widespread use of g-C$_3$N$_4$ as photocatalyst is its relatively poor quantum efficiency caused by the high recombination probability of photogenerated electron–hole pairs and lower specific surface area. In order to overcome these drawbacks, many attempts have been dedicated to improving the photocatalytic capability of g-C$_3$N$_4$, such as elemental doping [20,21], protonation [22], copolymerization of the nitrogen precursor [23] and composite [24], etc. Among these modified methods, combining with other materials to form composite photocatalysts is dominant because this technique can effectively inhibit the recombination of photogenerated charges. Besides, due to the

diversity of composite sources and the simplification and feasibility of experimental operation, a host of composite catalysts coupling with g-C$_3$N$_4$ have been successfully reported, such as graphene/g-C$_3$N$_4$ [25], N-TiO$_2$/g-C$_3$N$_4$ [26], g-C$_3$N$_4$/Cu$_2$O [27] and SnS$_2$/g-C$_3$N$_4$ [28], etc.

More recently, much research work has been reported on the influence of the structure of the composite photocatalysts on the visible light absorption, the photoinduced charge separation and the photocatalytic activity, therefore, the synthesis of composite photocatalysts with well-defined sizes and shapes has attracted extensive interest. Till date, various composites with controlled morphologies, such as nanotubes [29], nanofibers [30], hollow spheres [31] and core–shell nanostructures [32], have been prepared by a variety of preparative routes. In particular, the preparation of core–shell nanostructured materials is considered as a promising method to extremely enhance the visible light-harvesting efficiency and photocatalytic activity. It is because that this kind of architecture structure has the ability to promote interface combination and enhance charge transport capability of composites [32]. Meanwhile, the core/shell structure also can improve the stability and dispersibility of the composites, as well as meet some special requirements for the composite materials, such as shrinking the consumption of certain rare materials [33]. However, according to our knowledge, there are only few reports on studying the coupling mode of g-C$_3$N$_4$ with SiO$_2$ nanoparticles until now. Shalom et al. [34] prepared the SiO$_2$/g-C$_3$N$_4$ composite materials by co-pyrolysis of different weight ratios of dicyandiamide and SiO$_2$ nanoparticles. Wang et al. [35] have reported similar study that they have synthesized the SiO$_2$/g-C$_3$N$_4$ composite by heating a mixture of SiO$_2$ nanoparticles and melamine. However, the morphologies of these obtained SiO$_2$/g-C$_3$N$_4$ catalysts only show grain structure, and the effect of specific architecture structure on photocatalytic activity was not considered. Simultaneously, the actual photocatalytic mechanism of those SiO$_2$/g-C$_3$N$_4$ composites is unclear so far.

In this work, novel SiO$_2$/g-C$_3$N$_4$ core–shell nanospheres were synthesized by annealing the mixture of silica nanospheres and molten cyanamide (CA) molecules in nitrogen atmosphere, whose aim was to further improve the visible-light-induced photocatalytic activity of g-C$_3$N$_4$. The obtained composite photocatalysts were characterized by a variety of techniques, and the photocatalytic activity was evaluated by decomposing rhodamine B solution under visible light irradiation. The charge-transfer process on the interface of the core–shell nanospheres and the photocatalytic mechanism for the degradation of RhB over the SiO$_2$/g-C$_3$N$_4$ core–shell nanospheres were discussed in detail simultaneously.

2. Experimental

2.1. Material synthesis

All reagents for synthesis and analysis were commercially available and used without further treatment.

2.1.1. Synthesis of SiO$_2$ nanospheres
The SiO$_2$ nanospheres were prepared according to our previously reported method [36]. Typically, 10 mL tetraethyl orthosilicate (TEOS) was added to 90 mL ethanol under vigorous stirring to form solution A, meanwhile, 10 mL aqueous ammonia and 20 mL deionized water were added to 70 mL ethanol under vigorous stirring to form solution B. Next, solution A and solution B were mixed, constantly stirred and then heated at 40 °C for 2.5 h. The obtained silicon collosol was then centrifuged by a table-top low speed centrifuge (4000 rpm for 10 min) with 20 mL of plastic centrifuge tubes, washed two times with distilled water and once with ethanol. The final milky SiO$_2$ nanospheres with the average diameter of 200–300 nm can be obtained by drying the above-mentioned collosol at 80 °C in a drying oven overnight.

2.1.2. Synthesis of pure g-C$_3$N$_4$
2 g CA was directly calcined at 550 °C for 4 h in a tube furnace with a heating ramp of 2.3 °C min^{-1} in nitrogen atmosphere, the resultant canary yellow powder was collected for the further use.

2.1.3. Synthesis of the SiO$_2$/g-C$_3$N$_4$ core–shell nanospheres
In a typical procedure, different mass ratios of SiO$_2$ nanospheres and CA molecules were mixed at 70 °C for 2 h to allow molten CA molecules to adequately contact with SiO$_2$ nanospheres. Being cooled to indoor temperature, the mixture was grinded and then heated at 550 °C for 4 h in a tube furnace with a heating ramp of 2.3 °C min^{-1} in nitrogen atmosphere. The canary yellow samples can be obtained following this way. The obtained samples with different initial SiO$_2$ nanospheres and CA mass ratios of 1:1, 1.25:1, 1.5:1, 1.75:1 and 2:1 were denoted as SC-1, SC-2, SC-3, SC-4 and SC-5, respectively. For comparison, the referenced SiO$_2$/g-C$_3$N$_4$ composite sample was synthesized by the same approach, which only using commercial SiO$_2$ particles to replace the self-made SiO$_2$ nanospheres in the preparation, and the sample thus obtained was denoted as C- SiO$_2$/g-C$_3$N$_4$. In the meanwhile, a mechanically mixed SC-3 sample was also prepared by finely grinding 0.075 g SiO$_2$ nanospheres and 0.050 g g-C$_3$N$_4$ particles.

2.2. Characterization

The geometry and morphology of the as-prepared photocatalysts were characterized by using field-emission scanning electron microscope (JEOL, JSM-6700F) and transmission electron microscopy (JEOL, JEM-2100). The crystalline structure and phase component of the samples were collected by using powder X-ray diffraction (XRD; SHIMADZU, Lab X XRD-6000). Fourier transform infrared (FT-IR) spectra were applied on a Nicolet Avatar 360 FT-IR with the potassium bromide tablet method. UV–vis diffuse reflectance spectra (DRS) were detected in a Hitachi U-4100 UV–vis spectrometer with a lab-sphere diffuse reflectance accessory. The nitrogen adsorption-desorption isotherm curves of the as-prepared photocatalysts were measured using a BET analyzer (ASAP 3000), and the samples were degassed at 160 °C for 10 h before the actual measurement. The specific surface area and porosity of the samples were assessed on the basis of the Brunauer–Emmett–Teller (BET) equation and Barrett–Joyner–Halenda (BJH) method, respectively. The photoluminescence (PL) emission spectra were recorded on a HORIBA JY Fluorolog-3 type fluorescence spectrophotometer with 340 nm excitation wavelength.

2.3. Photocatalytic test

The photocatalytic activities of the so-fabricated photocatalysts were evaluated by photodegrading RhB dye which was used to simulate contaminated water under visible light irradiation. The light source was 300 W Xenon lamp (HSX-F300, Beijing NBeT) equipped with UV filter (HSX-UV300). Meanwhile, a cut-off glass filter ($\lambda \geq 420$ nm) was employed to eliminate UV light and admit only visible light to remain. The distance between the xenon lamp and the RhB solution was fixed to be 10 cm. Prior to the photoreaction, 70 mL aqueous solution of RhB dye (10 mg/L) containing 0.07 g the so-fabricated photocatalysts were magnetically stirred in the dark for 40 min to reach adsorption/desorption equilibrium. During illumination, 3 mL of the solution was withdrawn from the reactor every 30 min, the photocatalysts were then separated from the solution by centrifugation in a table-top high speed centrifuge with 1.5 mL of plastic centrifuge tubes (H1650-W, 10,000 rpm for

5 min), and the concentration of the remaining RhB solution was measured by UV–vis spectrophotometer (UV-1900PPC, Shanghai, China), and the maximum absorption wavelength of RhB is 554 nm. The remaining RhB concentration (x) could be calculated by the following formulation:

$$x = \frac{C}{C_0} \times 100\%$$

where C_0 is the initial concentration of RhB (achieving adsorption/desorption equilibrium), while C is the residual concentration of RhB after each illumination at specific times.

To further measure the reusability and stability of the sample with the best photocatalytic activity, the recycled experiments were performed as follows: 70 mL aqueous solution of RhB dye solution (10 mg/L) containing 0.07 g SC-3 sample were added to the above-mentioned photoreaction reactor and magnetically stirred in the dark for 40 min to reach adsorption/desorption equilibrium. The applied photoreaction procedure was the same as above described. After every 2.5 h photoreaction, the sample was isolated from the residual RhB solution and washed and dried for 4 h at 80 °C. Then the dried sample was added back to the photoreaction reactor to degrade the same volume of RhB dye solution (10 mg/L). Such operations were repeated 4 times under the same conditions. For comparison, the reusability of pure g-C₃N₄ was also measured in the recycled experiment under the same reaction conditions. In addition, the quenching experiments of the active species were also carried out to identify the main reactive species for the degradation of RhB solution (10 mg/L) over the SC-3 sample. Different scavengers, including disodium ethylenediaminetetraacetate dehydrate (EDTA-2Na, 10 mM), benzoquinone (BQ, 1 mM) and 2-propanol (IPA, 10 mM), were added to the above-mentioned mixed RhB solution before illumination to scavenge the h^+, $\bullet O_2^-$ and $\bullet OH$, respectively.

3. Results and discussion

The specific synthetic process of the core–shell nanosphere samples is illustrated in Fig. 1. Firstly, SiO₂ nanospheres were fabricated using a modified Stöber's method [36]. In the initial step, tetraethyl orthosilicate (TEOS) was stirred in the mixed solution of ethanol and deionized water, which could be easily hydrolyzed and condensed to gradually form SiO₂ nanospheres with uniform size in the presence of aqueous ammonia at 40 °C, meanwhile, a number of −OH groups can be produced and remained on the surface of SiO₂ nanospheres in this process. In the second
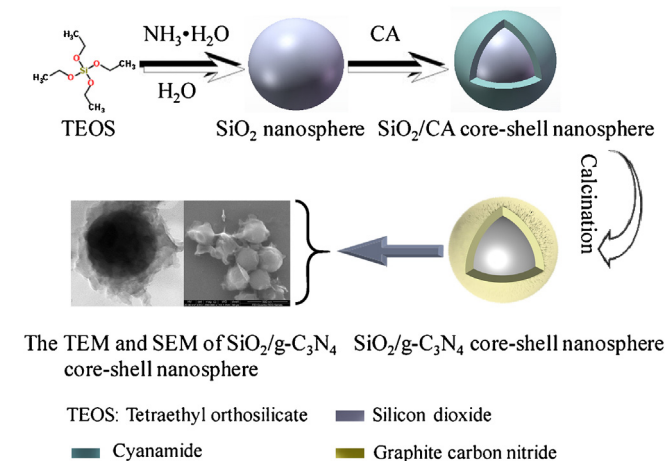
step, when the as-prepared SiO₂ nanospheres mixed with CA liquid by stirring at 70 °C, the existed surface −OH group can be reacted quickly with −NH₂ group which derived from cyanamide molecules (N≡C−NH₂), and thus the exterior of SiO₂ nanospheres could be tightly wrapped by CA molecules through the weak coordination interactions and hydrogen bonding, resulting in the formation of the SiO₂/CA core–shell nanospheres. In the third step, the post-treatment of calcination was followed to obtain the final SiO₂/g-C₃N₄ core–shell nanosphere photocatalysts, this process can effectively make the CA molecules transform into g-C₃N₄ through the transformation roadmap of cyanamide to dicyandiamide and later to melamine and g-C₃N₄ with the rise of the calcination temperature [6]. Simultaneously, calcination also leads to the formation of extremely close interfaces between g-C₃N₄ and SiO₂ nanospheres, which are beneficial for the improvement of photogenerated charge separation efficiency.

Fig. 2 shows the typical X-ray diffraction data for the as-prepared pure g-C₃N₄ sample, SiO₂ nanospheres and the SiO₂/g-C₃N₄ core–shell nanospheres with varying mass ratios of SiO₂ nanospheres and CA molecules in the initial materials. As shown in Fig. 2a, two diffraction peaks can be observed in the XRD pattern, which clearly correspond to the crystal phases of pure g-C₃N₄ sample. It should be noted that the stronger peak appeared at 2θ of 27.58° can be attributed to the (0 0 2) crystal plane of g-C₃N₄, which arises from the interlayer stacking of aromatic segments [37,38], while the weaker peak at 2θ of 13.07° can be assigned to the (1 0 0) crystal plane of g-C₃N₄, which is due to the repetitive in-plane structure motifs [29,39], for instance the hole-to-hole distance of tri-s-triazine units in graphitic carbon nitride [37,40]. Furthermore, as a whole, the diffraction peaks of pure g-C₃N₄ showed a
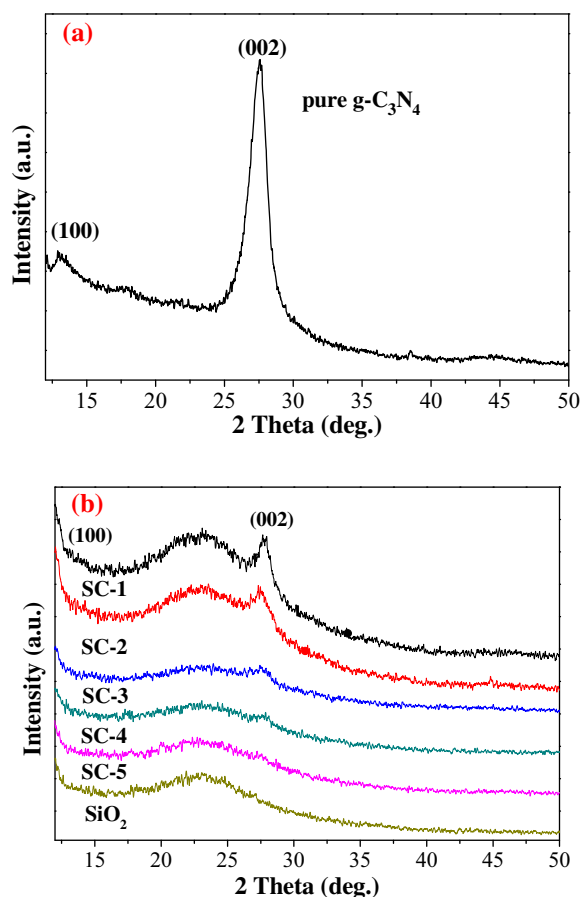
Fig. 1. Schematic illustration of the synthetic procedure of the SiO₂/g-C₃N₄ core–shell nanospheres.

Fig. 2. X-ray diffraction patterns of (a) pure g-C₃N₄ and (b) SiO₂ nanospheres and the SiO₂/g-C₃N₄ core–shell nanospheres.

prominent and sharp trend, suggestive of a superior crystalline degree. Fig. 2b illustrates the X-ray diffraction data for SiO_2 nanospheres and the SiO_2/g-C_3N_4 core–shell nanospheres with varying mass ratios. For SiO_2 sample, the broad peak appeared at 2θ of around 23° corresponded to amorphous structure of SiO_2 [35]. And all the SiO_2/g-C_3N_4 core–shell composites show the similar XRD patterns. Besides the broad peak for the SiO_2 phase, a relatively narrow peak located at 2θ of around 27.6° can be observed, which can be assigned to the (0 0 2) crystal plane of g-C_3N_4. In addition, it can be noted that the main (0 0 2) Bragg peak of graphitic carbon nitride gradually became weaker and broader with the increase of the mass ratios of SiO_2 nanospheres and CA molecules, and nearly disappeared in the SC-5 sample. Meanwhile, the peaks appeared at 2θ of around 13.1° denoted as the (1 0 0) crystal plane of g-C_3N_4 is quite hard to be observed in the XRD pattern, this signified that only low amount of g-C_3N_4 coated on the surface of SiO_2 nanospheres to form core–shell nanostructure. No other impure peaks can be found in the XRD data, suggestive of a two-phase composition of SiO_2 and g-C_3N_4 in these composites. For further confirming the core–shell structure, the SEM and TEM analysis were applied as following.

Fig. 3 shows the FE-SEM images of the SiO_2/g-C_3N_4 core–shell nanospheres with varying mass ratios of SiO_2 nanospheres and CA molecules, together with SiO_2 nanospheres and pure g-C_3N_4 sample. It can be seen from Fig. 3a that the silica sample displays uniform nanosphere structure with the average diameter of 200–300 nm, and these SiO_2 nanospheres have extremely smooth surface,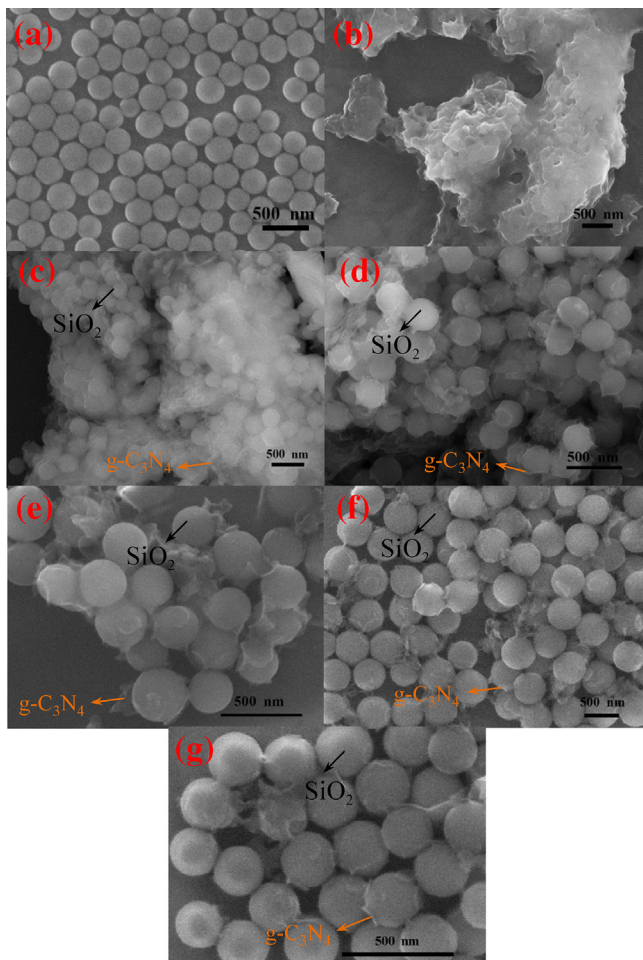 which contacted with each other to form an aggregate under SEM conditions. As shown in Fig. 3b, the initial g-C_3N_4 sample presents a typical lamellar structure, which is formed through aggregating of massive g-C_3N_4 particles. Fig. 3c–g show the typical SEM images of the SiO_2/g-C_3N_4 core–shell nanospheres. It can be observed that all the SiO_2/g-C_3N_4 composites have similar geometrical features. Some of sheet-like g-C_3N_4 particles were curled and thus covered on the surface of SiO_2 nanosphere to harvest a representative SiO_2/g-C_3N_4 core–shell microstructure. Herein, to carefully observe these SEM images of the SiO_2/g-C_3N_4 composites, a little difference still can be found in morphology. For SC-1 sample (Fig. 3c), the g-C_3N_4 layers have fully covered the exterior of SiO_2 nanospheres, this is because that a large number of CA molecules existed in the initial system, which could participate the reaction and eventually transfer into g-C_3N_4 particles. With the reduction of CA content, the thickness of g-C_3N_4 shell on the SiO_2 nanospheres surface decreased gradually, even partial surface of SiO_2 nanospheres was exposed to air, indicating that only a small amount of g-C_3N_4 was obtained in the case of the lower SiO_2/CA mass ratio. These results are in accordance with the XRD analysis.

The TEM measurement was further carried out to investigate the morphology and microstructures of the as-prepared samples. As illustrated in Fig. 4a, the TEM image of pure g-C_3N_4 shows that the sample has the obviously wrinkled two-dimensional structure, which is approximately 1.0–1.2 μm in width, 1.6–1.8 μm in length. Meanwhile, the TEM images of the five SiO_2/g-C_3N_4 composite samples further confirm that the wrinkled two-dimensional g-C_3N_4 flakes have covered well on the surface of SiO_2 nanospheres. With the changed content of CA in the starting materials, no obvious difference of size and morphology among these five SiO_2/g-C_3N_4 composites can be observed and all the obtained samples show a typical core–shell nanostructure. This is well consistent with the SEM observations. Moreover, the TEM images clearly reveal that an extremely close interface between SiO_2 nanospheres and g-C_3N_4 in the composites was formed, which is favorable for the transfer of photogenerated electrons from the surface of g-C_3N_4 to the surface

Fig. 3. SEM images of (a) SiO_2 nanospheres; (b) pure g-C_3N_4; (c) SC-1; (d) SC-2; (e) SC-3; (f) SC-4 and (g) SC-5.
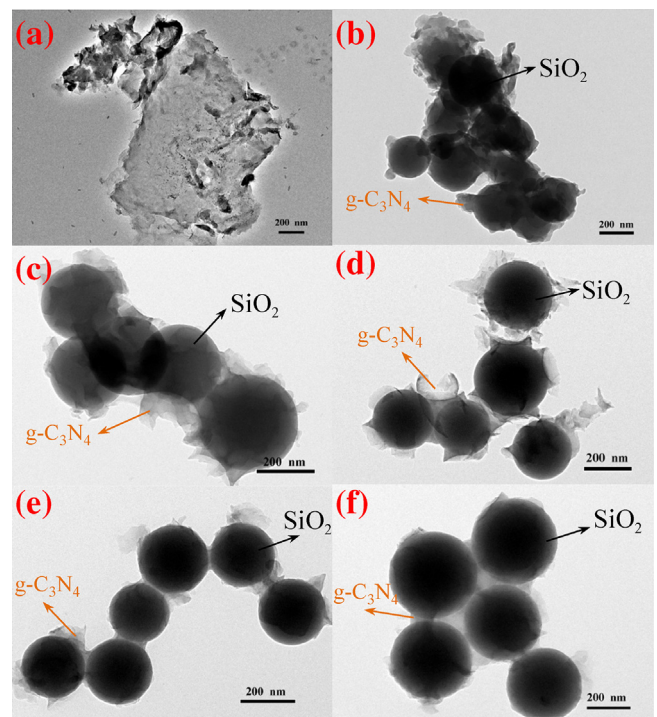

Fig. 4. TEM images of (a) pure g-C_3N_4; (b) SC-1; (c) SC-2; (d) SC-3; (e) SC-4 and (f) SC-5.

of SiO_2 nanospheres [35,41], as result of leading to the enhancement of photocatalytic activity.

Fig. 5 shows the FT-IR spectra of the SiO_2/g-C_3N_4 core–shell nanospheres with varying mass ratios of SiO_2 nanospheres and CA molecules, and the FT-IR spectra of pure g-C_3N_4 and SiO_2 nanospheres, used here as reference, were also shown in Fig. 5. It can be observed that there are four characteristic IR absorption regions in the FT-IR spectrum of the pure g-C_3N_4 sample. The bands centered at around $810 cm^{-1}$ and in the $1200–1700 cm^{-1}$ region can be ascribed to the breathing vibration of triazine ring motifs and the stretching vibration of CN heterocycles [31,37,38]. Besides, a minor band appeared at $2140 cm^{-1}$ correspond to the accumulated double bond (indicating N=N=N or N=C=N) as well as triple bond (indicating C≡N) of pure g-C_3N_4 [5]. The broad band located at $3100–3300 cm^{-1}$ can be assigned to the residual N—H bond originating from the secondary and primary amines and O—H band originating from adsorbed H_2O molecules [37,42]. In the case of pure SiO_2 nanospheres, the band at around $1100 cm^{-1}$ is attributed to the stretching vibration of Si—O—Si, the appearance of band at around $810 cm^{-1}$ was due to the bending vibration of Si—OH [43]. Furthermore, the band at around $1640 cm^{-1}$ was related to the bending and stretching vibrations of O—H, and the band at around $3400 cm^{-1}$ belonged to OH^- and the absorbed H_2O molecules [44]. When g-C_3N_4 attached on the surface of SiO_2 nanospheres to form composites, it can be noted that all the samples present similar FT-IR spectra, which show typical mixed molecular structure of g-C_3N_4 and SiO_2 nanospheres. However, a new peak at $2250 cm^{-1}$ was seen in the FT-IR spectra of SiO_2/g-C_3N_4 core–shell nanospheres, which is due to the accumulated double bond and triple bond of tri-s-triazine units [5], and a red shift of $110 cm^{-1}$ can be observed in comparison with the peak at $2140 cm^{-1}$ of pure g-C_3N_4, this can be attributed to the effect of coupling g-C_3N_4 with SiO_2 nanospheres to form the core–shell structure.

As shown in Fig. 6, the information on the optical properties of pure g-C_3N_4 and the SiO_2/g-C_3N_4 core–shell nanospheres prepared with varying mass ratios of SiO_2 nanospheres and CA was acquired using the UV–vis diffuse reflectance spectra. It can be seen that pure g-C_3N_4 has apparent absorption in the visible light region and its fundamental absorption edge can be observed to be 453 nm, which corresponds to its intrinsic band gap of 2.74 eV [45,46], in accordance with the bulk g-C_3N_4 mentioned in previous paper [47]. Compared with pure g-C_3N_4, the obtained SiO_2/g-C_3N_4 core–shell nanospheres show much stronger optical response ability, as a result, a red shift in the optical absorption edge of the samples into the visible light region, at 463 nm, was observed, which corresponds to the band gap of 2.68 eV for the SiO_2/g-C_3N_4
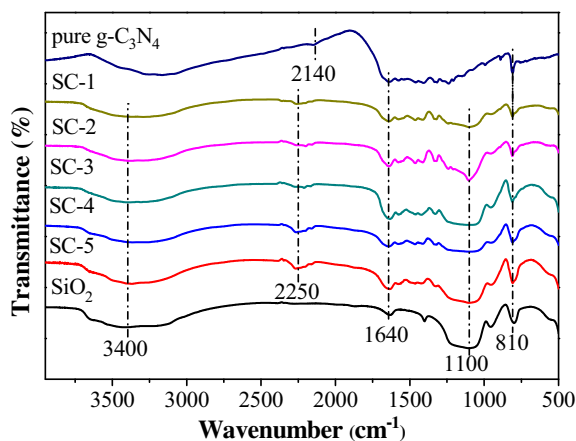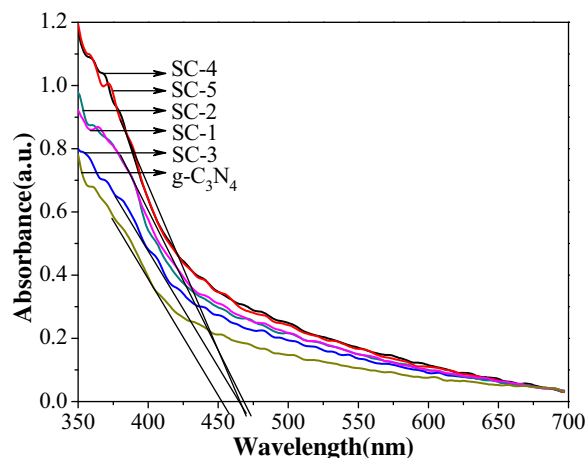
Fig. 6. UV–vis diffuse reflectance spectra of pure g-C_3N_4 and the SiO_2/g-C_3N_4 core–shell nanospheres.

composites. This phenomenon can be ascribed to the photosensitization effect of g-C_3N_4, and a bit narrower energy band gap may be due to the formation of compact interface and stronger combination between SiO_2 nanospheres and g-C_3N_4. We know that the thinner g-C_3N_4 layers coated on the surface of SiO_2 nanospheres can shorten the propagation distance of the photogenerated electrons and holes and thereby promote the separation of the photogenerated electron–hole pairs. In the meanwhile, the SiO_2 combined with g-C_3N_4 could extend the range of visible-light response and boost the utilization of light source; both of them take a big step forward on the photocatalytic activity. What's more, after coupling, it can be observed that the intensity of the absorption feature in the UV region for these composite samples becomes intense gradually, suggesting that the formation of core–shell structure leads to a beneficial effect on the optical absorption ability in the UV and visible-light regions for the as-prepared samples.

Fig. 7 shows the nitrogen adsorption-desorption isotherms of pure g-C_3N_4, SiO_2 nanospheres and the SiO_2/g-C_3N_4 core–shell nanospheres with varying mass ratios of SiO_2 nanospheres and CA molecules. All adsorption–desorption isotherms are similar and can be attributed to type IV isotherm with hysteresis loops on the basis of the IUPAC classification, implying the presence of representative mesoporous structure in the samples [48,49]. Furthermore, the conspicuous absorption hysteresis loop located at $0.7 < P/P_0 < 0.99$ with a flat "S"-shape in the isotherms could be
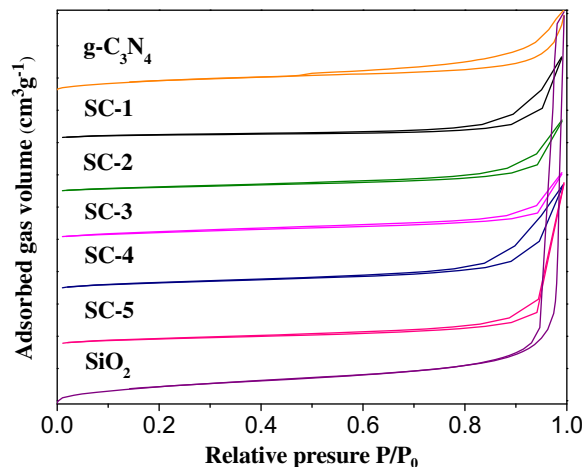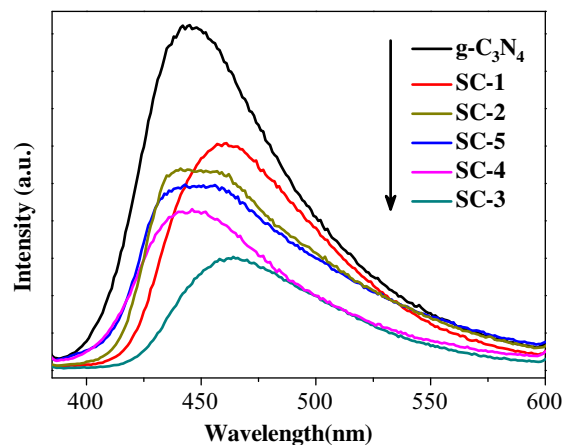
Fig. 5. FT-IR spectra of pure g-C_3N_4, SiO_2 nanospheres and the SiO_2/g-C_3N_4 core–shell nanospheres.

Fig. 7. Nitrogen adsorption–desorption isotherms of pure g-C_3N_4, SiO_2 nanospheres and the SiO_2/g-C_3N_4 core–shell nanospheres.

Table 1
Chemical compositions and textural properties of pure g-C$_3$N$_4$, SiO$_2$ nanospheres and the SiO$_2$/g-C$_3$N$_4$ core–shell nanospheres.

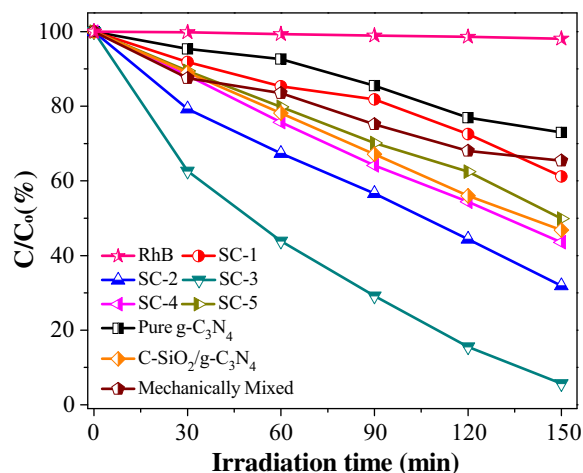| Samples	CA amount (wt.%)	SiO$_2$ amount (wt.%)	BET surface area (m^2 g^{-1})	Pore diameter (nm)	Pore volume (cm^3 g^{-1})
SiO$_2$	0	100	22.31	34.19	0.18
g-C$_3$N$_4$	100	0	6.93	13.91	0.03
SC-1	50	50	8.05	24.23	0.03
SC-2	44.44	55.56	10.55	23.46	0.05
SC-3	40	60	12.67	16.46	0.07
SC-4	36.36	63.64	9.39	17.34	0.04
SC-5	33.33	66.67	7.28	21.89	0.03

classified as type-H1 hysteresis loop, further indicating the existence of interstitial holes in these core–shell nanospheres [50], which are formed by the organized aggregation of vast g-C$_3$N$_4$ particles. However, a little difference can be observed in the isotherm profile of SiO$_2$ nanospheres, it is clear that its absorption hysteresis loop is located at $0.9 < P/P_0 < 0.99$, suggestive of the presence of mesoporous structure with a broad porous distribution in this sample [35]. The BET surface area, pore volume, and average pore size of all samples were summarized in Table 1. As listed in Table 1, the SiO$_2$ nanosphere sample shows relatively broader pore diameter (34.19 nm), larger pore volume (0.18 cm^3 g^{-1}) and higher specific surface area (22.31 m^2 g^{-1}). Whereas the pure g-C$_3$N$_4$ shows relatively narrower pore diameter (13.91 nm), smaller pore volume (0.03 cm^3 g^{-1}) and lower specific surface area (6.93 m^2 g^{-1}), this is because the g-C$_3$N$_4$ sample possesses typical lamellar structure and only a small quantity of pores exist in the bulk of g-C$_3$N$_4$, leading to a low surface area of g-C$_3$N$_4$ sample. As can be seen from Table 1, the mass ratios of SiO$_2$ nanospheres and CA molecules have an obvious influence on the textural properties of these composite catalysts. The variation of the average pore diameter of these five samples presented a trend of valley. With the increase of the mass ratios of SiO$_2$ nanospheres and CA molecules, the value of the average pore diameter decreased from 24.23 nm to 16.46 nm firstly, and then increased from 16.46 nm to 21.89 nm. In contrast, the variation of pore volume of these five samples manifested a trend of crest, as shown, the value of the pore volume increased firstly and then decreased. It can be found that SC-3 sample has the largest pore volume with the value of 0.07 cm^3 g^{-1}. Meanwhile, the change of BET specific surface area for these SiO$_2$/g-C$_3$N$_4$ core–shell nanospheres is the same as that of pore volume. Among these samples, the SC-3 sample also shows the highest BET specific surface area with the value of 12.67 m^2 g^{-1}. According to the above analysis, the formation of core–shell structure could lead g-C$_3$N$_4$ particles to be well dispersed on the surface of silica nanaospheres and prompt the shell of g-C$_3$N$_4$ to become thinner, and the pore volume and specific surface areas of the SiO$_2$/g-C$_3$N$_4$ core–shell nanospheres were therefore increased, this process is beneficial to the adsorption and mass transfer of reactants in the core–shell nanaospheres as well as providing more reaction active sites.

To investigate the effect on the processes of trapping, transfer and recombination of the photogenerated charge carriers in the presence of SiO$_2$ nanospheres, the room temperature photoluminescence experiments of the as-prepared photocatalysts were performed. Fig. 8 shows the PL spectra of pure g-C$_3$N$_4$ and the SiO$_2$/g-C$_3$N$_4$ core–shell nanospheres. It can be observed that the PL spectra of these samples are similar. However, all the SiO$_2$/g-C$_3$N$_4$ core–shell nanospheres show a lower PL intensity in comparison with pure g-C$_3$N$_4$. It is well known that the PL intensity is positively correlated with the recombination probability of the photogenerated electron–hole pairs, thus affecting the photocatalytic performance correspondingly [51,52]. Therefore, as previously reported [35,53], the above results indicate that the addition of SiO$_2$ nanospheres has a positive effect on restraining the recombination of the photogenerated electron–hole pairs because the existence of defects and vacancy sites on the surface of SiO$_2$

Fig. 8. Room temperature PL spectra for pure g-C$_3$N$_4$ and the SiO$_2$/g-C$_3$N$_4$ core–shell nanospheres.

seems to act as electron trapped centers. It is noted that SC-3 sample shows the lowest PL intensity, indicative of the strongest charge transfer and separation efficiency among the SiO$_2$/g-C$_3$N$_4$ composites.

On basis of the above results, the photocatalytic activities of the as-prepared samples were assessed by the photodegradation of RhB solution of 10 mg/L under visible light irradiation at room temperature, the RhB dye was used here to simulate the contaminated water due to its high chemical stability and extensive application in textile industry. Before running the photoreaction, the black test experiments (photolysis of RhB dye) were carried out at the same conditions simultaneously. Fig. 9 shows the corresponding plots for the change of RhB concentration determined

Fig. 9. Photocatalytic degradation of RhB solution over pure g-C$_3$N$_4$, the SiO$_2$/g-C$_3$N$_4$ core–shell nanospheres, the C-SiO$_2$/g-C$_3$N$_4$ and the mechanically mixed SiO$_2$/g-C$_3$N$_4$ sample under visible light irradiation ($\lambda \geq 420$ nm). The original concentration of RhB solution is 10 mg/L. C, concentration; C_0, initial concentration.

from its characteristic absorption peak at 554 nm. As shown in Fig. 9, the results of the blank test revealed that the RhB is quite stable, and almost no degradation of RhB can be observed in the absence of the photocatalyst after 150 min of visible light irradiation. The pure $g-C_3N_4$ sample shows the inferior photodegradation activity with an RhB conversion of approximately 27% under the same visible light irradiation, indicating that the layered structure of $g-C_3N_4$ had lower quantum efficiency and thus limited its further practical application. However, compared with pure $g-C_3N_4$, all the $SiO_2/g-C_3N_4$ core–shell nanospheres prepared with varying mass ratios of SiO_2 nanospheres and CA molecules show a significantly enhanced activity in terms of the degradation of RhB, indicating that coupling SiO_2 nanospheres with $g-C_3N_4$ to yield a core–shell structure is an effective way to improve the photocatalytic activity of $g-C_3N_4$ owing to the increased separation efficiency of photogenerated charge carriers between the two individual components. Interestingly, the results in Fig. 9 show that the mass ratios of SiO_2 nanospheres and CA molecules in the initial materials have a significant effect on the photocatalytic performance. It can be observed that the activity first increases from SC-1 to SC-3, and then gradually decreases with continuous change of the mass ratios of SiO_2 nanospheres and CA molecules. Among these samples, SC-3 shows the highest photodegradation activity with an RhB conversion of 94.3% within 150 min irradiation, which is approximately 3.5 times higher than that of pure $g-C_3N_4$. It should be noted that although the SC-1 sample shows the lowest activity, it is still higher than that of pure $g-C_3N_4$.

In order to further investigate the effect of core–shell structure and close interface between SiO_2 and $g-C_3N_4$ in the photocatalytic system, the photodegradation of RhB over the mechanically mixed sample and $C-SiO_2/g-C_3N_4$ composite was performed under the same reaction conditions. As shown in Fig. 9, the mechanically mixed sample and $C-SiO_2/g-C_3N_4$ composite show a weak activity, and their RhB conversion is only 34% and 53.2%, respectively, within 150 min photoreaction. It can be found that the activities of the mechanically mixed sample and the $C-SiO_2/g-C_3N_4$ composite are slightly higher than that of pure $g-C_3N_4$, but much lower than that of the SC-3 sample. This phenomenon can be attributed to the significant difference in the interface of these photocatalysts. The TEM and SEM results show that a closely contacted interface between $g-C_3N_4$ and SiO_2 nanospheres can be formed in the core–shell system, whereas only a nonuniform interface was formed in mechanically mixed sample. As we all know, the closely contacted interface could lead to the charge transfer process become much more smooth and efficient. Furthermore, layered $g-C_3N_4$ nanosheet was wrapped on the exterior of SiO_2 nanospheres to obtain a core–shell structure, and the thickness of the $g-C_3N_4$ layer for these samples can be observed to be thinner comparable to that of pure $g-C_3N_4$, which contributes to a high surface area and thus induces better surface absorbability of superoxide radical ($•O_2^-$) and hydroxyl radical ($•OH$), which in-turn act as the active oxidizers in the photocatalytic reaction. In addition, as the results of PL spectra mentioned, the defects and vacancy sites on the surface of SiO_2 nanospheres simultaneously play an important role in capturing the photogenerated electrons, which is beneficial for promoting the separation of photogenerated electron–hole pairs and thus enhancing the photocatalytic activities of the $SiO_2/g-C_3N_4$ core–shell samples.

The above photocatalytic experiments have demonstrated that the sample of SC-3 possesses an excellent photocatalytic activity under visible light irradiation. However, as an efficient visible-light-driven photocatalyst, the performance of reuse and stability for the $SiO_2/g-C_3N_4$ core–shell nanospheres plays a vital role in the practical application. In this work, the recycled experiments were carried out to investigate the reusability of the as-prepared sample. Fig. 10a shows the recycling test of pure $g-C_3N_4$ and the SC-3 sample for photocatalytic degradation of RhB solution of 10 mg/L under
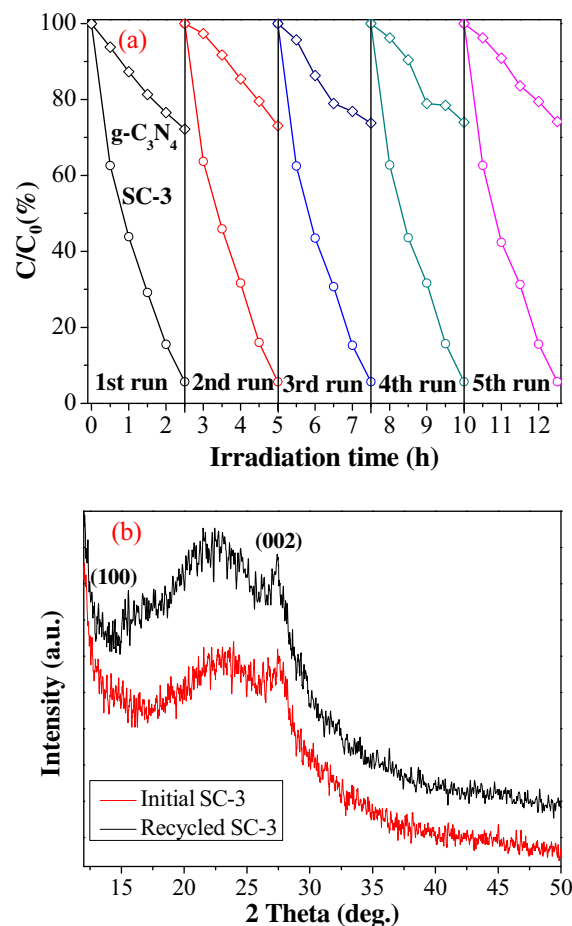

Fig. 10. (a) The cycling runs of the degradation of RhB solution (10 mg/L) over pure $g-C_3N_4$ and SC-3 under visible light irradiation; (b) X-ray diffraction patterns of the initial SC-3 sample and the recycled SC-3 sample (after 5th photoreaction).

visible light irradiation. After five cycling runs of photodegradation of RhB, the photocatalytic performance of pure $g-C_3N_4$ slightly reduces from an RhB conversion of 27.7% to approximately 26% within 150 min photoreaction, while the SC-3 sample still remains the higher photocatalytic performance and the RhB solution can be completely degraded within 150 min photoreaction. It is can be observed that the stability and durability of core–shell nanospheres have been significantly improved than pure $g-C_3N_4$ due to the addition of SiO_2. In addition, it should be noted that the formation of core–shell structure with nano-spherical shape offers an excellent ability that the present $SiO_2/g-C_3N_4$ composites can be facilely separated from an aqueous system, which thus indicates an outstanding potential for the application of sustainable energy and photoreaction. Fig. 10b shows the XRD patterns of SC-3 sample before and after 5th photoreaction. It can be easily observed that the XRD curves of the sample of the initial SC-3 and the recycled SC-3 sample which underwent five cycling experiments of photodegradation of RhB are extremely similar with the same diffraction peaks, this can effectively demonstrate the phase stability of the $SiO_2/g-C_3N_4$ photocatalysts, conforming to the results of the recycled experiments.

In order to shed light on the main reactive species in the process of photodegradation of RhB, the effects of different scavengers on the degradation of RhB solution over SC-3 were studied. In our experiments, EDTA-2Na, BQ and IPA were used as scavenger to quench h^+, $•O_2^-$ and $•OH$, respectively [54,55]. As shown in Fig. 11, the photocatalytic degradation rate for RhB can reach up to 94.3% without any scavengers within 150 min irradiation. Besides, the
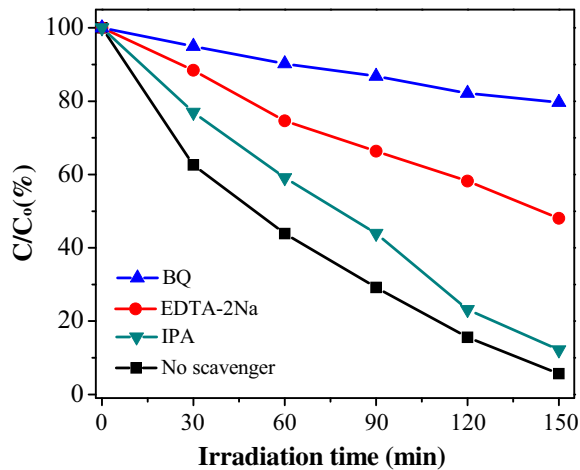
Fig. 11. Effects of different scavengers on the degradation of RhB solution (10 mg/L) over SC-3.

addition of IPA slightly suppressed the decolorization of RhB, and the photocatalytic degradation rate for RhB reduced to 87.9%, indicating that the role of •OH played was extremely limited in the process of photodegradation of RhB. On the contrary, the photocatalytic degradation process of RhB was greatly influenced with the addition of EDTA-2Na or BQ, and the photocatalytic degradation rate for RhB reduced to 52.0% and 20.3%, respectively, suggesting that h[+] and •O$_2^-$ are the main reactive species rather than •OH radical in the process of photodegradation of RhB.

On the basis of the above results of quenching experiments of active species, we tentatively put forward a transfer process of the photogenerated charges on the interface of the core–shell nanospheres and a photocatalytic mechanism of degrading RhB solution over the SiO$_2$/g-C$_3$N$_4$ composites under visible light irradiation. Fig. 12 shows the schematic illustration of the photocatalytic process for RhB decomposition on the as-prepared photocatalysts. As shown in Fig. 12, the detailed charge transfer process can be described as follow: when the synthesized SiO$_2$/g-C$_3$N$_4$ composites were illuminated under visible light, the g-C$_3$N$_4$ was motivated to generate charge carriers, and then the photoexcited electrons

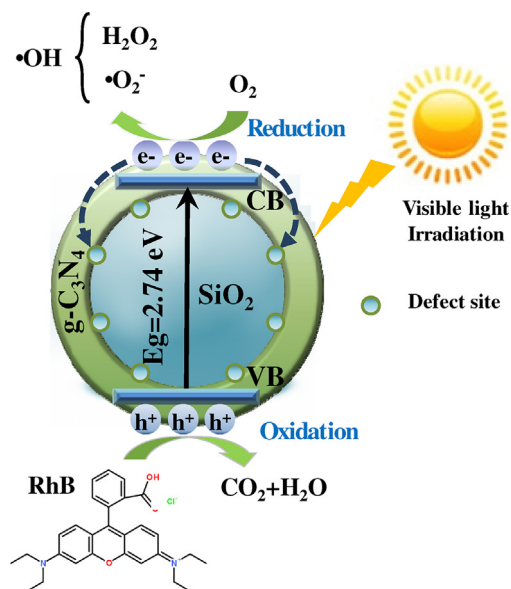leaped from the valence band (VB) of g-C$_3$N$_4$ to the conduction band (CB) of itself, while the corresponding photoexcited holes remained on the VB of g-C$_3$N$_4$. It is conscious that the photoexcited electrons or holes could not move to the band gap of SiO$_2$ because of the mismatched band potentials (The energy band gaps of SiO$_2$ and g-C$_3$N$_4$ are 9.0 eV [56] and 2.74 eV, respectively), however, as the previously reported [35,53,57], these photoexcited electrons can directly transfer to the SiO$_2$ surface through the closely contacted interfaces, and be trapped by the defect and vacancy sites which existed on the surface of SiO$_2$ nanospheres. This process can effectively inhibit the possibility of photoexcited charges recombination, allowing more opportunities for photoexcited electrons and holes to participate in the oxidation-reduction reactions, thus resulting in the high photocatalytic activity and stability of the SiO$_2$/g-C$_3$N$_4$ composites.

In addition, as previously reported, the reduction potential (−1.22 eV vs. NHE) of the photoexcited electrons derived from the CB of g-C$_3$N$_4$ was more negative than that of O$_2$/•O$_2^-$ (−0.33 eV vs. NHE) [32,58], so the photoexcited electrons would react with the adsorbed O$_2$ on the surface of the photocatalysts to produce superoxide radical (•O$_2^-$) and hydrogen peroxide (H$_2$O$_2$), and the two new species could further react to form the hydroxyl radical (•OH) [36]. Both •O$_2^-$ and •OH possess the superior ability of degrading RhB. Here, it should be noted that the reduction potential of the photoexcited holes on the VB of g-C$_3$N$_4$ (+1.51 eV vs. NHE) was not positive enough than that of •OH/OH$^-$ (+1.99 eV vs. NHE) [32,58], and thus the hydroxyl radical (•OH) can be not directly produced by the interaction between the photoexcited holes on the VB of g-C$_3$N$_4$ and the absorbed H$_2$O molecules or hydroxyl (OH$^-$) on the surface of the photocatalysts [58,59]. However, the photoexcited holes also could participate in the redox reaction to decompose RhB. Hence, the highly efficient degradation of RhB in this work is the combined action of •OH, •O$_2^-$ and the photoexcited holes, but the latter two species play major roles in the photoreaction.

From the above discussion, we tentatively concluded that the enhancement of photocatalytic activity for RhB degradation over the SiO$_2$/g-C$_3$N$_4$ core–shell nanospheres can be attributed to the following points. Firstly, the SEM and TEM images have been shown that the lamellar g-C$_3$N$_4$ was well covered on the surface of SiO$_2$ nanospheres to form a core–shell structure, and the thickness of the g-C$_3$N$_4$ layer was quite thin, which could shorten the propagation distance of the photogenerated charges from the g-C$_3$N$_4$ bulk to the g-C$_3$N$_4$ surface, this process can promote much more photogenerated electrons and holes to take part in the photoreaction. Secondly, with the formation of core–shell structure, the pore volumes and the specific surface areas of the SiO$_2$/g-C$_3$N$_4$ core–shell nanospheres were therefore increased (as shown in Table 1), as a result of benefiting the adsorption and mass transfer of reactants in the core–shell nanaospheres as well as providing more reaction active sites. Thirdly, based on the previous studies [35,53,57] and our experimental data, the extremely close interfaces between SiO$_2$ nanospheres and g-C$_3$N$_4$ in the composites can be formed, and the defect and vacancy sites on the surface of SiO$_2$ nanospheres could capture the photogenerated electrons through the closely contacted interfaces, this process can effectively restrain the recombination of photogenerated electron–hole pairs. Finally, the stronger visible light absorption of the SiO$_2$/g-C$_3$N$_4$ core–shell nanospheres is also beneficial for the enhancement of activity for the photocatalysts (UV–vis DRS data).

4. Conclusion

In conclusion, the SiO$_2$/g-C$_3$N$_4$ core–shell nanospheres were synthesized by annealing the mixture of silica nanospheres and molten cyanamide in nitrogen atmosphere. Photocatalytic

Fig. 12. Schematic illustration of RhB degradation over the SiO$_2$/g-C$_3$N$_4$ core–shell nanospheres under visible light irradiation.

experiments revealed that the photocatalytic activity of the composite samples were far more superior than that of pure g-C_3N_4. Among these as-prepared catalysts, the SC-3 sample had the highest photodegradation activity with an RhB conversion of 94.3% within 150 min of visible light irradiation, which is approximately 3.5 times higher than that of pure g-C_3N_4. And the cycling runs of the degradation of RhB solution showed that the SC-3 sample possessed outstanding stability and durability.

Acknowledgements

References

[1] A. Kudo, Y. Miseki, Heterogeneous photocatalyst materials for water splitting, Chem. Soc. Rev. 38 (2009) 253–278.

[2] B. Liu, L.M. Liu, X.F. Lang, H.Y. Wang, X.W. Lou, E.S. Aydil, Doping high-surface-area mesoporous TiO_2 microspheres with carbonate for visible light hydrogen production, Energy Environ. Sci. 7 (2014) 2592–2597.

[3] J. Fu, B.B. Chang, Y.L. Tian, F.N. Xi, X.P. Dong, Novel C_3N_4-CdS composite photocatalysts with organic-inorganic heterojunctions: in situ synthesis, exceptional activity, high stability and photocatalytic mechanism, J. Mater. Chem. A 1 (2013) 3083–3090.

[4] H.B. Wu, H.H. Hng, X.W. Lou, Direct synthesis of anatase TiO_2 nanowires with enhanced photocatalytic activity, Adv. Mater. 24 (2012) 2567–2571.

[5] E.G. Gillan, Synthesis of nitrogen-rich carbon nitride networks from an energetic molecular azide precursor, Chem. Mater. 12 (2000) 3906–3912.

[6] Y. Wang, X.C. Wang, M. Antonietti, Polymeric graphitic carbon nitride as a heterogeneous organocatalyst: from photochemistry to multipurpose catalysis to sustainable chemistry, Angew. Chem. Int. Ed. 51 (2012) 68–89.

[7] X.C. Wang, K. Maeda, A. Thomas, K. Takanabe, G. Xin, J.M. Carlsson, K. Domen, M. Antonietti, A metal-free polymeric photocatalyst for hydrogen production from water under visible light, Nat. Mater. 8 (2009) 76–80.

[8] J. Wang, W.D. Zhang, Modification of TiO_2 nanorod arrays by graphite-like C_3N_4 with high visible light photoelectrochemical activity, Electrochim. Acta 71 (2012) 10–16.

[9] F. Goettmann, A. Fischer, M. Antonietti, A. Thomas, Chemical synthesis of mesoporous carbon nitrides using hard templates and their use as a metal-free catalyst for Friedel–Crafts reaction of benzene, Angew. Chem. Int. Ed. 45 (2006) 4467–4471.

[10] F.Z. Su, M. Antonietti, X.C. Wang, Mpg-C_3N_4 as a solid base catalyst for Knoevenagel condensations and transesterification reactions, Catal. Sci. Technol. 2 (2012) 1005–1009.

[11] X.J. Ye, Y.J. Cui, X.Q. Qiu, X.C. Wang, Selective oxidation of benzene to phenol by Fe-CN/TS-1 catalysts under visible light irradiation, Appl. Catal. B: Environ. 152–153 (2014) 383–389.

[12] X.S. Zhang, J.Y. Hu, H. Jiang, Facile modification of a graphitic carbon nitride catalyst to improve its photoreactivity under visible light irradiation, Chem. Eng. J. 256 (2014) 230–237.

[13] D.J. Martin, K.P. Qiu, S.A. Shevlin, A.D. Handoko, X.W. Chen, Z.X. Guo, J.W. Tang, Highly efficient photocatalytic H_2 evolution from water using visible light and structure-controlled graphitic carbon nitride, Angew. Chem. Int. Ed. 53 (2014) 9240–9245.

[14] X.C. Wang, X.F. Chen, A. Thomas, X.Z. Fu, M. Antonietti, Metal-containing carbon nitride compounds: a new functional organic-metal hybrid material, Adv. Mater. 21 (2009) 1609–1612.

[15] X.C. Wang, K. Maeda, X.F. Chen, K. Takanabe, K. Domen, Y.D. Hou, X.Z. Fu, M. Antonietti, Polymer semiconductors for artificial photosynthesis: hydrogen evolution by mesoporous graphitic carbon nitride with visible light, J. Am. Chem. Soc. 131 (2009) 1680–1681.

[16] S.S. Park, S.W. Chu, C.F. Xue, D.Y. Zhao, C.S. Ha, Facile synthesis of mesoporous carbon nitrides using the incipient wetness method and the application as hydrogen adsorbent, J. Mater. Chem. 21 (2011) 10801–10807.

[17] S.P. Lee, J.G. Lee, S. Chowdhury, CMOS humidity sensor system using carbon nitride film as sensing materials, Sensors 8 (2008) 2662–2672.

[18] S.P. Lee, Synthesis and characterization of carbon nitride films for micro humidity sensors, Sensors 8 (2008) 1508–1518.

[19] V.D. Noto, E. Negro, Development of nano-electrocatalysts based on carbon nitride supports for the ORR processes in PEM fuel cells, Electrochim. Acta 55 (2010) 7564–7574.

[20] G. Liu, P. Niu, C.H. Sun, S.C. Smith, Z.G. Chen, G.Q. Lu, H.M. Cheng, Unique electronic structure induced high photoreactivity of sulfur-doped graphitic C_3N_4, J. Am. Chem. Soc. 132 (2010) 11642–11648.

[21] Y.J. Zhang, T. Mori, J.H. Ye, M. Antonietti, Phosphorus-doped carbon nitride solid: enhanced electrical conductivity and photocurrent generation, J. Am. Chem. Soc. 132 (2010) 6294–6295.

[22] Y.J. Zhang, A. Thomas, M. Antonietti, X.C. Wang, Activation of carbon nitride solids by protonation: morphology changes, enhanced ionic conductivity, and photoconduction experiments, J. Am. Chem. Soc. 131 (2009) 50–51.

[23] J.S. Zhang, X.F. Chen, K. Takanabe, K. Maeda, K. Domen, J.D. Epping, X.Z. Fu, M. Antonietti, X.C. Wang, Synthesis of a carbon nitride structure for visible-light catalysis by copolymerization, Angew. Chem. Int. Ed. 49 (2010) 441–444.

[24] Z.W. Tong, D. Yang, T.X. Xiao, Y. Tian, Z.Y. Jiang, Biomimetic fabrication of g-C_3N_4/TiO_2 nanosheets with enhanced photocatalytic activity toward organic pollutant degradation, Chem. Eng. J. 260 (2015) 117–125.

[25] Q.J. Xiang, J.G. Yu, M. Jaroniec, Preparation and enhanced visible-light photocatalytic H_2-production activity of graphene/C_3N_4 composites, J. Phys. Chem. C 115 (2011) 7355–7363.

[26] X.J. Wang, W.Y. Yang, F.T. Li, Y.B. Xue, R.H. Liu, Y.J. Hao, In situ microwave-assisted synthesis of porous N-TiO_2/g-C_3N_4 heterojunctions with enhanced visible-light photocatalytic properties, Ind. Eng. Chem. Res. 52 (2013) 17140–17150.

[27] B.Y. Peng, S.S. Zhang, S.Y. Yang, H.J. Wang, H. Yu, S.Q. Zhang, F. Peng, Synthesis and characterization of g-C_3N_4/Cu_2O composite catalyst with enhanced photocatalytic activity under visible light irradiation, Mater. Res. Bull. 56 (2014) 19–24.

[28] Z.Y. Zhang, J.D. Huang, M.Y. Zhang, Q. Yuan, B. Dong, Ultrathin hexagonal SnS_2 nanosheets coupled with g-C_3N_4 nanosheets as 2D/2D heterojunction photocatalysts toward high photocatalytic activity, Appl. Catal. B: Environ. 163 (2015) 298–305.

[29] J. Gao, Y. Zhou, Z.S. Li, S.C. Yan, N.Y. Wang, Z.G. Zou, High-yield synthesis of millimetre-long, semiconducting carbon nitride nanotubes with intense photoluminescence emission and reproducible photoconductivity, Nanoscale 4 (2012) 3687–3692.

[30] M. Tahir, C.B. Cao, N. Mahmood, F.K. Butt, A. Mahmood, F. Idrees, S. Hussain, M. Tanveer, Z. Ali, I. Aslam, Multifunctional g-C_3N_4 nanofibers: a template-free fabrication and enhanced optical, electrochemical, and photocatalyst properties, ACS Appl. Mater. Interfaces 6 (2014) 1258–1265.

[31] J.H. Sun, J.S. Zhang, M.W. Zhang, M. Antonietti, X.Z. Fu, X.C. Wang, Bioinspired hollow semiconductor nanospheres as photosynthetic nanoparticles, Nat. Commun. 3 (2012) 1139.

[32] S. Kumar, A. Baruah, S. Tonda, B. Kumar, V. Shanker, B. Sreedhar, Cost-effective and eco-friendly synthesis of novel and stable N-doped ZnO/g-C_3N_4 core–shell nanoplates with excellent visible-light responsive photocatalysis, Nanoscale 6 (2014) 4830–4842.

[33] R.G. Chaudhuri, S. Paria, Core/shell nanoparticles: classes, properties, synthesis mechanisms, characterization, and applications, Chem. Rev. 112 (2012) 2373–2433.

[34] M. Shalom, S. Inal, D. Neher, M. Antonietti, SiO_2/carbon nitride composite materials: the role of surfaces for enhanced photocatalysis, Catal. Today 225 (2014) 185–190.

[35] X.X. Wang, S.S. Wang, W.D. Hu, J. Cai, L.H. Zhang, L.Z. Dong, L.H. Zhao, Y.M. He, Synthesis and photocatalytic activity of SiO_2/g-C_3N_4 composite photocatalyst, Mater. Lett. 115 (2014) 53–56.

[36] C. Xue, T. Wang, G.D. Yang, B.L. Yang, S.J. Ding, A facile strategy for the synthesis of hierarchical TiO_2/CdS hollow sphere heterostructures with excellent visible light activity, J. Mater. Chem. A 2 (2014) 7674–7679.

[37] Y.J. Cui, J.S. Zhang, G.G. Zhang, J.H. Huang, P. Liu, M. Antonietti, X.C. Wang, Synthesis of bulk and nanoporous carbon nitride polymers from ammonium thiocyanate for photocatalytic hydrogen evolution, J. Mater. Chem. 21 (2011) 13032–13039.

[38] F.T. Li, Y.B. Xue, B. Li, Y.J. Hao, X.J. Wang, R.H. Liu, J. Zhao, Precipitation synthesis of mesoporous photoactive Al_2O_3 for constructing g-C_3N_4-based heterojunctions with enhanced photocatalytic activity, Ind. Eng. Chem. Res. 53 (2014) 19540–19549.

[39] Y.J. Cui, J.H. Huang, X.Z. Fu, X.C. Wang, Metal-free photocatalytic degradation of 4-chlorophenol in water by mesoporous carbon nitride semiconductors, Catal. Sci. Technol. 2 (2012) 1396–1402.

[40] F. Goettmann, A. Fischer, M. Antonietti, A. Thomas, Metal-free catalysis of sustainable Friedel–Crafts reactions: direct activation of benzene by carbon nitrides to avoid the use of metal chlorides and halogenated compounds, Chem. Commun. (2006) 4530–4532.

[41] F.T. Li, Y. Zhao, Y.J. Hao, X.J. Wang, R.H. Liu, D.S. Zhao, D.M. Chen, N-doped P25 TiO_2-amorphous Al_2O_3 composites: one-step solution combustion preparation and enhanced visible-light photocatalytic activity, J. Hazard. Mater. 239–240 (2012) 118–127.

[42] X.H. Li, J.S. Zhang, X.F. Chen, A. Fischer, A. Thomas, M. Antonietti, X.C. Wang, Condensed graphitic carbon nitride nanorods by nanoconfinement: promotion of crystallinity on photocatalytic conversion, Chem. Mater. 23 (2011) 4344–4348.

[43] X.M. Tai, Z.P. Du, W.X. Wang, M.F. Hou, Y.H. Zhao, The one-step method preparation of thermal responsive SiO_2/poly-ether composites, Powder Technol. 264 (2014) 273–277.

[44] T. Wang, X.Q. Yan, S.S. Zhao, B. Lin, C. Xue, G.D. Yang, S.J. Ding, B.L. Yang, C.S. Ma, G. Yang, G.R. Yang, A facile one-step synthesis of three-dimensionally ordered macroporous N-doped TiO_2 with ethanediamine as the nitrogen source, J. Mater. Chem. A 2 (2014) 15611–15619.

[45] X. Xu, G.R. Yang, J. Liang, S.J. Ding, C.L. Tang, H.H. Yang, W. Yan, G.D. Yang, D.M. Yu, Fabrication of one-dimensional heterostructured TiO_2@SnO_2 with enhanced photocatalytic activity, J. Mater. Chem. A 2 (2014) 116–122.

[46] G.D. Yang, Z.F. Yan, T.C. Xiao, B.L. Yang, Low-temperature synthesis of alkalis doped TiO_2 photocatalysts and their photocatalytic performance for degradation of methyl orange, J. Alloys Compd. 580 (2013) 15–22.

[47] S. Kumar, B. Kumar, T. Surendar, V. Shanker, g-C_3N_4/$NaTaO_3$ organic-inorganic hybrid nanocomposite: high-performance and recyclable visible light driven photocatalyst, Mater. Res. Bull. 49 (2014) 310–318.

[48] J.Y. Zhang, Y.H. Wang, J. Jin, J. Zhang, Z. Lin, F. Huang, J.G. Yu, Efficient visible-light photocatalytic hydrogen evolution and enhanced photostability of core/shell CdS/g-C_3N_4 nanowires, ACS Appl. Mater. Interfaces 5 (2013) 10317–10324.

[49] X. Lin, X.Y. Guo, W.L. Shi, F. Guo, H.J. Zhai, Y.S. Yan, Q.W. Wang, Ag_3PO_4 quantum dots sensitized $AgVO_3$ nanowires: a novel Ag_3PO_4/$AgVO_3$ nanojunction with enhanced visible-light photocatalytic activity, Catal. Commun. 66 (2015) 67–72.

[50] X.J. Ye, Y. Zheng, X.C. Wang, Synthesis of ferrocene-modified carbon nitride photocatalysts by surface amidation reaction for phenol synthesis, Chin. J. Chem. 32 (2014) 498–506.

[51] F. Guo, W.L. Shi, X. Lin, X. Yan, Y. Guo, G.B. Che, Novel $BiVO_4$/$InVO_4$ heterojunctions: facile synthesis and efficient visible-light photocatalytic performance for the degradation of rhodamine B, Sep. Purif. Technol. 141 (2015) 246–255.

[52] X. Lin, X.Y. Guo, W.L. Shi, L.N. Zhao, Y.S. Yan, Q.W. Wang, Ternary heterostructured Ag-$BiVO_4$/$InVO_4$ composites: synthesis and enhanced visible-light-driven photocatalytic activity, J. Alloys Compd. 635 (2015) 256–264.

[53] X. Lin, X.Y. Guo, D. Liu, Q.W. Wang, H.J. Zhai, L.M. Chang, SiO_2/Bi_2MoO_6 nanocomposites with high photocatalytic activity under visible light irradiation, Mater. Res. Bull. 63 (2015) 72–79.

[54] F.T. Li, S.J. Liu, Y.B. Xue, X.J. Wang, Y.J. Hao, J. Zhao, R.H. Liu, D.S. Zhao, Structure modification function of g-C_3N_4 for Al_2O_3 in the in situ hydrothermal process for enhanced photocatalytic activity, Chem. Eur. J. 21 (2015) 10149–10159.

[55] Y.J. Yao, J.C. Qin, H. Chen, F.Y. Wei, X.T. Liu, J.L. Wang, S.B. Wang, One-pot approach for synthesis of N-doped TiO_2/$ZnFe_2O_4$ hybrid as an efficient photocatalyst for degradation of aqueous organic pollutants, J. Hazard. Mater. 291 (2015) 28–37.

[56] J.B. You, X.W. Zhang, H.P. Song, J. Ying, Y. Guo, A.L. Yang, Z.G. Yin, N.F. Chen, Q.S. Zhu, Energy band alignment of SiO_2/ZnO interface determined by X-ray photoelectron spectroscopy, J. Appl. Phys. 106 (2009) 043709.

[57] F.T. Li, Y. Zhao, Q. Wang, X.J. Wang, Y.J. Hao, R.H. Liu, D.S. Zhao, Enhanced visible-light photocatalytic activity of active Al_2O_3/g-C_3N_4 heterojunctions synthesized via surface hydroxyl modification, J. Hazard. Mater. 283 (2015) 371–381.

[58] W.J. Wang, J.C. Yu, D.H. Xia, P.K. Wong, Y.C. Li, Graphene and g-C_3N_4 nanosheets cowrapped elemental α-sulfur as a novel metal-free heterojunction photocatalyst for bacterial inactivation under visible-light, Environ. Sci. Technol. 47 (2013) 8724–8732.

[59] T. Xian, H. Yang, L.J. Di, J.F. Dai, Enhanced photocatalytic activity of $BaTiO_3$@g-C_3N_4 for the degradation of methyl orange under simulated sunlight irradiation, J. Alloys Compd. 622 (2015) 1098–1104.